GEOLOGY | THE GEOLOGICAL SOCIETY OF AMERICA®

https://doi.org/10.1130/G46631.1

Manuscript received 13 June 2019
Revised manuscript received 11 September 2019
Manuscript accepted 18 November 2019

Published online 3 January 2020

Ecological disturbance in tropical peatlands prior to marine Permian-Triassic mass extinction

Daoliang Chu[1]*, Stephen E. Grasby[2], Haijun Song[1], Jacopo Dal Corso[3], Yao Wang[1], Tamsin A. Mather[4], Yuyang Wu[1], Huyue Song[1], Wenchao Shu[1], Jinnan Tong[1] and Paul B. Wignall[3]*

[1]State Key Laboratory of Biogeology and Environmental Geology, School of Earth Sciences, China University of Geosciences, Wuhan 430074, China

[2]Geological Survey of Canada, Natural Resources Canada, Calgary, Alberta T2L 2A7, Canada

[3]School of Earth and Environment, University of Leeds, Leeds LS2 9JT, UK

[4]Department of Earth Sciences, University of Oxford, South Parks Road, Oxford OX1 3AN, UK

ABSTRACT

The Permian-Triassic mass extinction is widely attributed to the global environmental changes caused by the eruption of the Siberian Traps. However, the precise temporal link between marine and terrestrial crises and volcanism is unclear. Here, we report anomalously high mercury (Hg) concentrations in terrestrial strata from southwestern China, synchronous with Hg anomalies in the marine Permian-Triassic type section. The terrestrial sediments also record increased abundance of fossil charcoal coincident with the onset of a negative carbon isotope excursion and the loss of tropical rainforest vegetation, both of which occurred immediately before the peak of Hg concentrations. The organic carbon isotope data show an ~5‰–6‰ negative excursion in terrestrial organic matter (bulk organic, cuticles, and charcoal), reflecting change in atmospheric CO_2 carbon-isotope composition coincident with enhanced wildfire indicated by increased charcoal. Hg spikes provide a correlative tool between terrestrial and marine records along with carbon isotope trends. These data demonstrate that ecological deterioration occurred in tropical peatlands prior to the main marine mass extinction.

INTRODUCTION

The Permian-Triassic mass extinction (PTME) was the most severe extinction event of the Phanerozoic, both in marine and terrestrial settings (Wignall, 2015), but the relative timing of these crises is debated (e.g., S.Z. Shen et al., 2011; Gastaldo et al., 2015; Fielding et al., 2019). A negative carbon isotope excursion (CIE) in both carbonate and organic matter (OM) is seen at the main extinction horizon and is usually attributed to release of volcanic carbon (Korte et al., 2010; Cui et al., 2013). Most proposed kill mechanisms are linked to the effects of Siberian Traps eruptions (Wignall, 2001; Grasby et al. 2011). A spike in mercury (Hg) concentrations observed at the onset of the PTME, thought to be derived from Siberian eruptions, provides a chemostratigraphic marker in marine records (Sanei et al., 2012; Grasby et al., 2013; Wang et al., 2018, 2019; J. Shen et al., 2019a). A similar Hg enrichment event has also been documented in contemporaneous terrestrial sediments (J. Shen et al., 2019b).

Marine records show widespread environmental instability prior to the PTME (e.g., S.Z. Shen et al., 2019), and a new study of the Sydney Basin (New South Wales, Australia), suggests that the collapse of southern high-latitude floras occurred significantly before the onset of marine extinctions (Fielding et al., 2019), roughly coincident with onset of northern high-latitude marine stress (Grasby et al., 2011, 2015).

To evaluate the timing and nature of the terrestrial crisis, we examined variations in fossil charcoal abundance from paleo–tropical peatland in southwestern China to explore changes in wildfire occurrence (e.g., Scott, 2010), and the carbon-isotope composition ($\delta^{13}C_{org}$) of land plant cuticles, charcoal, and bulk OM to track changes in the isotopic composition of atmospheric CO_2 (Arens et al., 2000; Schneebeli-Hermann et al., 2013). In addition, we investigated sedimentary Hg concentrations, and integration of our Hg record with carbon isotope values permits chemostratigraphic correlation of terrestrial and marine records.

STUDY AREA

We examined the continental Permian-Triassic (P-Tr) transition in cored borehole ZK4703, drilled 15 km south of Fuyuan County, China (25.54151°N, 104.28994°E), and the Chinahe outcrop section, 30 km southeastern of Xuanwei City (26.13077°N, 104.35637°E), both from the border area between western Guizhou and eastern Yunnan in southwestern China (Fig. 1; Fig. DR1 in the GSA Data Repository[1]). Latest Permian to earliest Triassic terrestrial strata in this region include, in ascending order, the fluvial-coastal swamp facies of the Xuanwei and Kayitou Formations (Chu et al., 2016; Zhang et al., 2016). The former consists of sandstone, mudstone, and common coal beds. The associated plant fossils belong to the *Gigantopteris* flora and include pecopterids, gigantopterids, lycopsiales, and equisetales taxa, collectively regarded as tropical rainforest-type vegetation (e.g., S.Z. Shen et al., 2011; Chu et al., 2016). The Kayitou Formation (latest Permian to earliest Triassic age) is similar to the underlying Xuanwei Formation, but lacks coal and is shale dominated. Previous studies showed that the loss of

*E-mails: chudl@cug.edu.cn; p.b.wignall@leeds.ac.uk

[1]GSA Data Repository item 2020079, descriptions of sample processing and studied sections, host of Hg in sediments, and supplementary figures and data tables, is available online at http://www.geosociety.org/datarepository/2020/, or on request from editing@geosociety.org.

CITATION: Chu, D., et al., 2020, Ecological disturbance in tropical peatlands prior to marine Permian-Triassic mass extinction: Geology, v. 48, p. 288–292, https://doi.org/10.1130/G46631.1

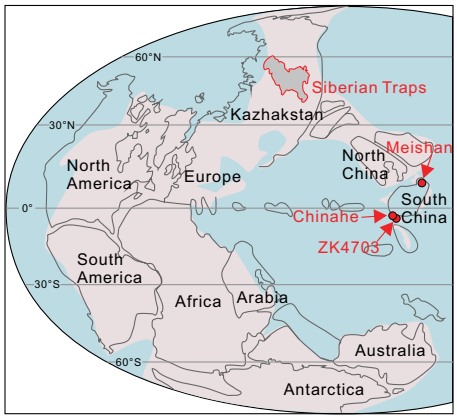

Figure 1. Late Permian to Early Triassic paleogeographic map showing locations of the ZK4703 core (25.54151°N, 104.28994°E) and the Chinahe section (26.13077°N, 104.35637°E) in southwestern China, and the Meishan section, south China (base map after Muttoni et al., 2009).

the *Gigantopteris* flora occurred in the lowest Kayitou Formation (Chu et al., 2016; Zhang et al., 2016).

METHODS

Organic carbon isotopes, charcoal abundance, fossil plant ranges, total organic carbon (TOC), total sulfur concentrations (TS), and aluminum (Al) and Hg contents were assessed through the P-Tr transition in the ZK4703 core and at the Chinahe outcrop. To avoid facies variation issues, only mudstone samples were processed for charcoal. Some charcoal was examined under scanning electron microscope (SEM) to confirm identification. To ensure that the charcoal concentrations were not affected by variations in the nature or abundance of organic material, its abundance was normalized to phytoclast abundance and TOC. The $\delta^{13}C_{org}$ values of decarbonated samples were analyzed using an elemental analyzer (EA) coupled with an isotope ratio mass spectrometer (Thermo Finnegan DeltaV). A Multi EA 4000 analyzer was used for TOC and TS determination. Hg content was measured using a LECO AMA254 mercury analyzer (ZK4703) and a Lumex RA-915 portable mercury analyzer with PYRO-915 pyrolyzer (Chinahe). Major element abundances were measured using an Agilent 7700e inductively coupled plasma–mass spectrometer. More sampling and laboratory details are given in the Data Repository.

RESULTS

Organic Carbon Isotopes

The $\delta^{13}C_{org}$ of bulk OM declines by –5‰ (from –25.2‰ to –30.2‰) in the lower part of the Kayitou Formation at Chinahe. Charcoal $\delta^{13}C_{org}$ values also decline from –24.5‰ to a minimum value of –29.5‰ in the lower part of the Kayitou Formation (Fig. 2B). For the ZK4703 core section, palynomorph color indicates stage 2–3 on the thermal alteration scale (Fig. DR2; Batten, 1996), demonstrating the cuticles' suitability for the carbon isotope investigation. The three ZK4703 $\delta^{13}C_{org}$ curves are similar (to each other and to the Chinahe record) and show a synchronous onset of a negative CIE, although absolute values differ (Fig. 2F): bulk OM–based and charcoal-based values are 1‰–2‰ heavier than the cuticle-based values. Overall, all the $\delta^{13}C_{org}$ records in the Xuanwei Formation initially show stable values around –25.5‰ to –24.5‰ before a decrease of ~5‰ in the lowest part of the Kayitou Formation.

Paleobotanical Record

The abundant, peat-forming *Gigantopteris* flora is seen at six levels in the Xuanwei Formation at Chinahe, and is dominated by well-preserved, large leaves (Fig. DR3). Both diversity and abundance of this flora decline drastically at the very top of the formation at a level that corresponds to the onset of the negative CIE (Fig. 2A; Fig. DR4). Thereafter, the flora consists of a monotonous assemblage of small plants, mostly *Annalepis* and *Peltaspermum*.

Charcoal Abundances

At Chinahe, the charcoal abundance is <300 particles per 100 g rock prior to the negative CIE, but rises briefly above background levels during the onset of the negative CIE (1524 particles per 100 g at 25 m log height), and ranges from 400 to 1600 particles per 100 g in the ~4 m interval of the uppermost part of the Xuanwei Formation to lower part of the Kayitou Formation (Fig. 2C). Similarly, in the ZK4703 record there is a sharp increase in charcoal abundance, from <400 particles per 100 g below 15 m, to >2400 particles per 100 g above 16.5 m height at the base of the Kayitou Formation (Fig. 2G). SEM observation shows that the charcoal preserves anatomical details (Fig. DR2) and has similar preservation and structures with variable size, indicating minimal transport sorting. The reported variations in charcoal abundance do not appear to be an artifact of preservation or changes in terrestrial organic delivery, because variations in preserved phytoclasts and TOC show little covariation with charcoal abundance (Fig. DR5).

Hg Concentrations and Hg/TOC Ratios

Mudstone TOC concentrations are relatively high (~1.5 wt%) in the Xuanwei Formation (varying from 0.4 to 2.8 wt% in Chinahe, and 0.8 to 3.1 wt% in ZK4703) and modestly enriched concentrations persist into the lower part of Kayitou Formation before dropping to 0.2–0.75 wt% at 17.5 m height in ZK4703 and 0.1–0.6 wt% at 27 m log height at Chinahe (Figs. 2D and 2H). Hg and Hg/TOC rise above background levels immediately above the interval with the onset of the CIE and increased charcoal abundance (Figs. 2E and 2I). High Hg concentrations and Hg/TOC can also be observed at higher stratigraphic levels, with a peak value at 19.75 m (324 ppb) in the ZK4703 core, which is ~50× background levels. Hg and Hg/TOC drop to the previous baseline values above 37 m at Chinahe and 25 m in ZK4703. The weak correlation between Hg and TOC concentrations (R^2 <0.05, P >0.05; Fig. DR6) suggests that the Hg fluctuations are not affected by changes in TOC. Additionally, the ZK4703 core has low total sulfur contents (mostly <0.15%) which show no significant covariation with Hg values (R^2 <0.01, P >0.05). Correlation between Al and Hg concentrations is also weak (R^2 <0.15, P <0.05), indicating that Hg fluctuations are not controlled primarily by clay content, even if some Hg is probably adsorbed onto clay. Nonetheless, there is secular variability in the Hg/Al ratio, with very low background Hg/Al values below and above the Hg anomaly and enriched Hg/Al values within the interval (Fig. DR7).

DISCUSSION

Hg Anomaly in the Terrestrial Setting of Southwestern China

Volcanic emissions represent one of the largest natural inputs of Hg to the atmosphere (Pirrone et al., 2010), and the Hg enrichment seen in many marine P-Tr boundary sequences is thought to record large-scale Siberian Traps eruptions (Sanei et al., 2012; Grasby et al., 2015, 2017; Wang et al., 2018). Volcanic Hg emissions from this source may have been up to 10,000 Mg yr^{-1} (~14× natural background; Grasby et al., 2015). Thermogenic release of Hg from baking of organic-rich sediments on contact with Siberian Traps intrusions is another potential source of Hg (Wang et al., 2019). Terrestrial plants constitute a large Hg reservoir, and so wildfires can also contribute significantly to Hg fluxes to the atmosphere and freshwater environments such as those studied here (e.g., Them et al., 2019). We propose that the Hg spikes observed in terrestrial (this work) and marine (Sanei et al., 2012; Grasby et al., 2015, 2017; Wang et al., 2018) successions provide a useful correlative tool between terrestrial and marine records along with $\delta^{13}C_{org}$ trends (Fig. 3).

The onset of the main phase of marine extinctions in South China, at the top of the *Clarkina yini* Zone, correlates with a peak in Hg concentrations and Hg/TOC, while a second phase of extinctions at the top of the *Isarcicella staeschi* Zone corresponds to a rise in Hg concentrations and Hg/TOC that peaks in the following *I. isarcica* Zone (Wang et al., 2018, 2019). The relative magnitude of these peaks varies between sections: at Meishan, South China, the lower Hg/TOC peak is the largest (Wang et al., 2018; Fig. 3), whereas at Guryul Ravine, Kashmir, the second peak is larger (Wang et al., 2019). $\delta^{13}C$

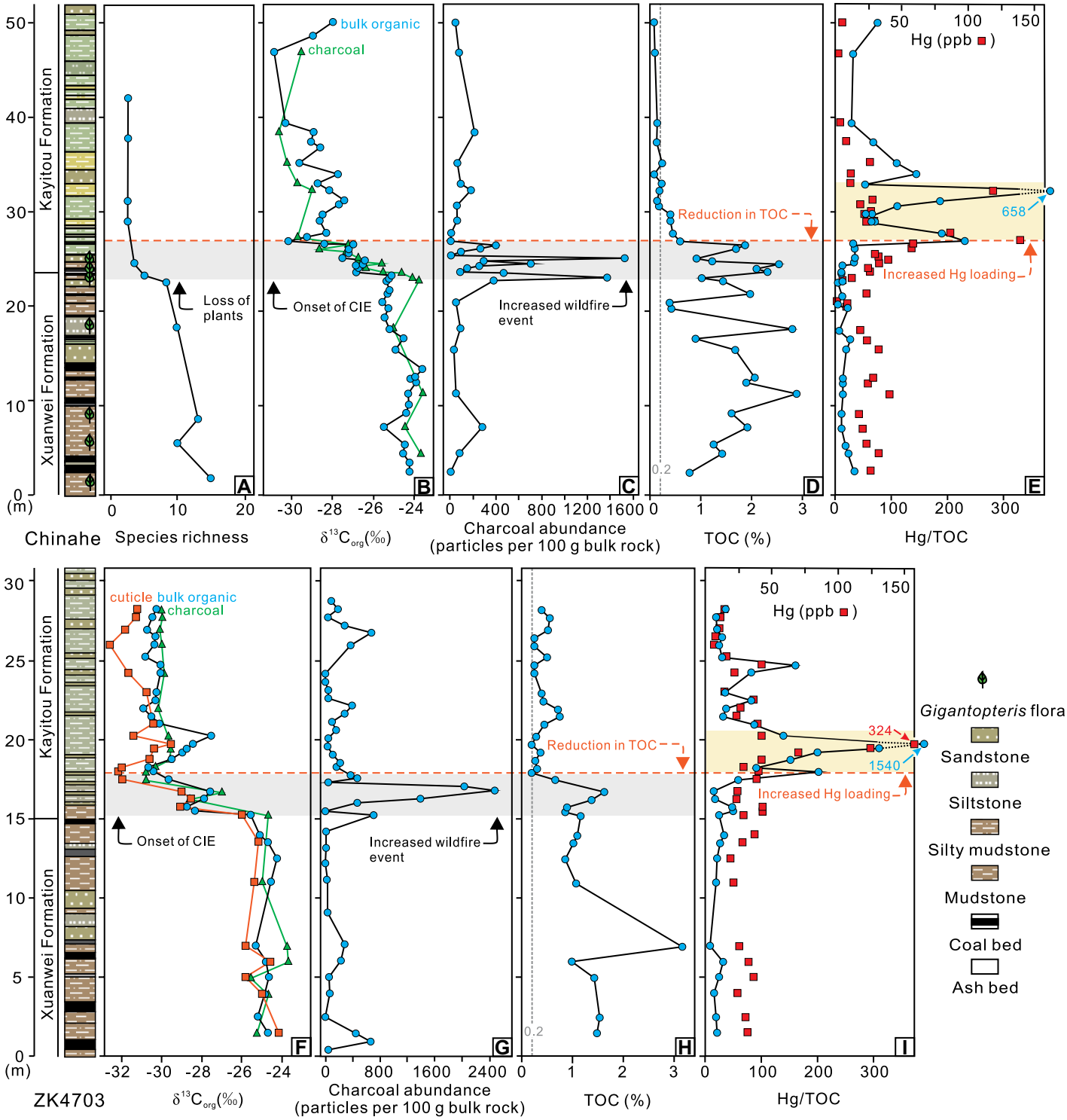

Figure 2. Stratigraphy, plant fossil species richness, organic carbon isotopes ($\delta^{13}C_{org}$), charcoal abundance, total organic carbon (TOC), Hg concentration, and Hg/TOC ratios in the Chinahe section (26.13077°N, 104.35637°E) and the ZK4703 core (25.54151°N, 104.28994°E), southwestern China. (A) Variation of plant fossil species richness (number of different species) of the Chinahe section. (B) Bulk organic matter and charcoal $\delta^{13}C$ records from Chinahe. (C) Variation of charcoal abundance (particles per 100 g bulk rock) from Chinahe. (D) Vertical trends in TOC values at Chinahe. (E) Vertical trends in Hg concentration and Hg/TOC ratios at Chinahe. (F) Bulk organic matter, cuticle, and charcoal $\delta^{13}C$ records from core ZK4703. (G) Variation of charcoal abundance (particles per 100 g bulk rock) from ZK4703. (H) Trends in TOC data from ZK4703. (I) Trends in Hg concentration and Hg/TOC data from ZK4703. Gray zones show onset of negative carbon isotope excursion (CIE) coupled with increased wildfire event. Yellow zones show enrichment Hg and Hg/TOC ratios. All data are given in the Data Repository (see footnote 1).

began to decline somewhat before the marine extinctions in the *Clarkina changxingensis* Zone (Fig. 3).

In the terrestrial sections of southwestern China, the floral mass extinction (and charcoal peak) starts with the onset of the CIE. Hg concentrations begin to slightly rise at the same time, while Hg/TOC shows a sharp spike at the minimum of the CIE (Fig. 2). The Hg and

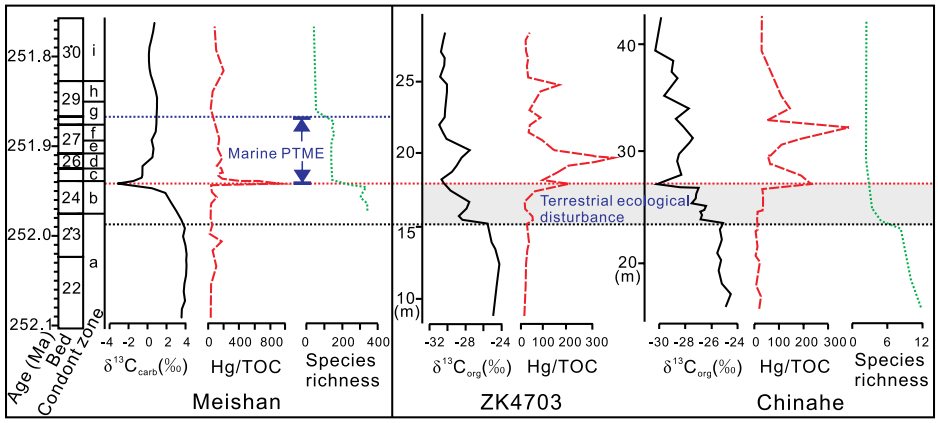

Figure 3. Carbon isotope and Hg/TOC (TOC—total organic carbon) correlations between marine Permian-Triassic global stratotype section at Meishan, China, and the two terrestrial sections studied here (the ZK4703 core and Chinahe section in southwestern China). $\delta^{13}C_{carb}$ (carb—carbonate) data for Meishan are from S.Z. Shen et al. (2011) and Burgess et al. (2017). Hg/TOC data for Meishan are from Grasby et al. (2017) and Wang et al. (2018). Species richness (number of different species) data for Meishan is from Song et al. (2013). Gray zone shows interval of terrestrial ecological disturbance. PTME—Permian-Triassic mass extinction; $\delta^{13}C_{org}$—organic $\delta^{13}C$. Conodont zones: a—*Clarkina changxingensis*; b—*C. yini*; c—*C. meishanensis*; d—*Hindeodus changxingensis*; e—*C.taylorae*; f—*H. parvus*; g—*Isarcicella staeschei*; h—*I.isarcica;* i—*C. planata*.

Hg/TOC peak 4–6 m above the terrestrial extinction level and likely correlate with the rise in Hg/TOC values seen at the end–*I. staeschi* Zone that saw diverse taxa disappear from Triassic oceans (Song et al., 2013). Thus, the terrestrial crisis seen in equatorial sections of China appears to predate the main marine extinction phase (which occurred near the low point of CIE), and likely dates to the late *C. changxingensis* Zone (Fig. 3).

Carbon Cycle Perturbation and Atmospheric Carbon Injection

Our results demonstrate that a synchronous onset of the negative CIE is present in the bulk OM, cuticle, and charcoal carbon isotope records from terrestrial settings (Fig. 2). Changes in $\delta^{13}C_{org}$ values of land plant cuticles record changes in atmospheric CO_2 (e.g., Schneebeli-Hermann et al., 2013). We suggest that the observed negative CIE in cuticles and fossil charcoal reflects an injection of ^{13}C-depleted emissions associated with the Siberian Traps. Interestingly, in our study, the peak in Hg concentrations and Hg/TOC ratios also occurred after the onset of the negative CIE (Fig. 2), suggesting a decoupling between the C and the Hg records that could result from the source of these two elements, be it volcanic, thermogenic, continental runoff, wildfire, or a combination of different reservoirs. Such decoupling deserves further investigation because it suggests different mechanisms of C and Hg release and/or processing in end-Permian environments.

Recurrent Wildfire and Climate Instability

Studies have shown insignificant or constant fractionation of carbon isotopes during the burning process, and so charcoal $\delta^{13}C$ values are a direct record of the original wood tissue $\delta^{13}C$ composition (e.g., Hall et al., 2008). The gradual decrease in the $\delta^{13}C$ of terrestrial plant-derived charcoal in the studied successions indicates, as discussed also for cuticle $\delta^{13}C$, a change in $\delta^{13}C$ of the original peat and vegetation due to changes in the $\delta^{13}C$ of the atmospheric CO_2. The charcoal $\delta^{13}C$ negative shift is coeval with an increase in charcoal abundance, i.e., with increased wildfire activity (Fig. 2), suggesting that the latest Permian forests experienced recurring wildfires and regrowth while the atmosphere became more ^{13}C depleted. Additionally, burning of terrestrial plant biomass can also increase the emission of Hg into the atmosphere, and then this Hg can be scavenged and buried in sediments (e.g., Grasby et al., 2017; Them et al., 2019).

The intensification of wildfire activity at the time of terrestrial mass extinction provides evidence of the harmful climatic changes in the lead-up to terrestrial crisis. The *Gigantopteris* coastal swamp flora thrived in humid, warm equatorial locations (S.Z. Shen et al., 2011) and was unlikely to have been adapted to intense levels of wildfire, as evidenced by the low charcoal abundance prior to the extinction interval (Figs. 2C and 2G). Thus, the increased wildfires suggest a transition to more unstable conditions punctuated by dry periods that would have been detrimental to coastal swamp floras (Zhang et al., 2016).

CONCLUSIONS

Our study sheds new light on the temporal links between the deterioration in the terrestrial environment and floral extinction, and the geochemical changes that mark the PTME. Our terrestrial Hg record from the P-Tr transition shows a sharp peak contemporaneous with the disappearance of Permian flora that correlates with marine Hg records. $\delta^{13}C$ data from cuticles and fossil charcoal, thought to reflect changes in the carbon isotope composition of the atmosphere, show an ~5‰–6‰ negative CIE during the terrestrial flora mass extinction interval. However, this was prior to the increase in Hg concentrations. Charcoal abundance shows that the floral extinctions coincided with an increase of wildfire activity and the carbon-cycle disruption. This likely reflects a change from persistent humidity to an unstable climate with frequent drought episodes. The temporal relationships between the events show that terrestrial disruption occurred shortly (but measurably) before the marine crisis.

ACKNOWLEDGMENTS

We are very grateful to David Bond, Thierry Adatte, and an anonymous reviewer for their constructive comments, and to editor Mark Quigley for handling our paper. This study was supported by the National Natural Science Foundation of China (grants 41530104, 41661134047, 41702015) and the UK Natural Environment Research Council's Eco-PT project (grant NE/P01377224/1), which is a part of the Biosphere Evolution, Transitions and Resilience (BETR) Program.

REFERENCES CITED

Arens, N.C., Jahren, A.H., and Amundson, R., 2000, Can C3 plants faithfully record the carbon isotopic composition of atmospheric carbon dioxide?: Paleobiology, v. 26, p. 137–164, https://doi.org/10.1666/0094-8373(2000)026<0137:CCPFRT>2.0.CO;2.

Batten, D.J., 1996, Palynofacies and petroleum potential, *in* Jansonius, J., and McGregor, D.C., eds., Palynology: Principles and Applications: Dallas, Texas, American Association of Stratigraphic Palynologists Foundation, p. 1065–1084.

Burgess, S.D., Muirhead, J.D., and Bowring, S.A., 2017, Initial pulse of Siberian Traps sills as the trigger of the end-Permian mass extinction: Nature Communications, v. 8, 164, https://doi.org/10.1038/s41467-017-00083-9.

Chu, D.L., Yu, J.X., Tong, J.N., Benton, M.J., Song, H.J., Huang, Y.F., Song, T., and Tian, L., 2016, Biostratigraphic correlation and mass extinction during the Permian-Triassic transition in terrestrial-marine siliciclastic settings of South China: Global and Planetary Change, v. 146, p. 67–88, https://doi.org/10.1016/j.gloplacha.2016.09.009.

Cui, Y., Kump, L.R., and Ridgwell, A., 2013, Initial assessment of the carbon emission rate and climatic consequences during the end-Permian mass extinction: Palaeogeography, Palaeoclimatology, Palaeoecology, v. 389, p. 128–136, https://doi.org/10.1016/j.palaeo.2013.09.001.

Fielding, C.R., et al., 2019, Age and pattern of the southern high-latitude continental end-Permian extinction constrained by multiproxy analysis: Nature Communications, v. 10, 385, https://doi.org/10.1038/s41467-018-07934-z.

Gastaldo, R.A., Kamo, S.L., Neveling, J., Geissman, J.M., Bamford, M., and Looy, C.V., 2015, Is the vertebrate-defined Permian-Triassic boundary in the Karoo Basin, South Africa, the terrestrial expression of the end-Permian marine

event?: Geology, v. 43, p. 939–942, https://doi.org/10.1130/G37040.1.
Grasby, S.E., Sanei, H., and Beauchamp, B., 2011, Catastrophic dispersion of coal fly ash into oceans during the latest Permian extinction: Nature Geoscience, v. 4, p. 104–107, https://doi.org/10.1038/ngeo1069.
Grasby, S.E., Sanei, H., Beauchamp, B., and Chen, Z., 2013, Mercury deposition through the Permo-Triassic Biotic Crisis: Chemical Geology, v. 351, p. 209–216, https://doi.org/10.1016/j.chemgeo.2013.05.022.
Grasby, S.E., Beauchamp, B., Bond, D.P.G., Wignall, P.B., Talavera, C., Galloway, J.M., Piepjohn, K., Reinhardt, L., and Blomeier, D., 2015, Progressive environmental deterioration in northwestern Pangea leading to the latest Permian extinction: Geological Society of America Bulletin, v. 127, p. 1331–1347, https://doi.org/10.1130/B31197.1.
Grasby, S.E., Shen, W., Yin, R., Gleason, J.D., Blum, J.D., Lepak, R. F., Hurley, J.P., and Beauchamp. B., 2017, Isotopic signatures of mercury contamination in latest Permian oceans: Geology, v. 45, p. 55–58, https://doi.org/10.1130/G38487.1.
Hall, G., Woodborne, S., and Scholes, M., 2008, Stable carbon isotope ratios from archaeological charcoal as palaeoenvironmental indicators: Chemical Geology, v. 247, p. 384–400, https://doi.org/10.1016/j.chemgeo.2007.11.001.
Korte, C., Pnade, P., Kalle, P., Kozur, H.W., Joachimski, M.M., and Oberhänsli, H., 2010, Massive volcanism at the Permian-Triassic boundary and its impact on the isotopic composition of the ocean and atmosphere: Journal of Asian Earth Sciences, v. 37, p. 293–311, https://doi.org/10.1016/j.jseaes.2009.08.012.
Muttoni, G., Gaetani, M., Kent, D.V., Sciunnach, D., Angiolini, L., Berra, F., Garzanti, E., Mattei, M., and Zanchi, A., 2009, Opening of the Neo-Tethys Ocean and the Pangea B to Pangea A transformation during the Permian: GeoArabia, v. 14, p. 17–48.
Pirrone, N., et al., 2010, Global mercury emissions to the atmosphere from anthropogenic and natural sources: Atmospheric Chemistry and Physics Discussion, v. 10, p. 4719–4752, https://doi.org/10.5194/acpd-10-4719-2010.
Sanei, H., Grasby, S.E., and Beauchamp, B., 2012, Latest Permian mercury anomalies: Geology, v. 40, p. 63–66, https://doi.org/10.1130/G32596.1.
Schneebeli-Hermann, E., Kürschner, W.M., Hochuli, P.A., Ware, D., Weissert, H., Bernasconi, S.M., Roohi, G., ur-Rehman, K., Goudemand, N., and Bucher, H., 2013, Evidence for atmospheric carbon injection during the end-Permian extinction: Geology, v. 41, p. 579–582, https://doi.org/10.1130/G34047.1.
Scott, A.C., 2010, Charcoal recognition, taphonomy and uses in palaeoenvironmental analysis: Palaeogeography, Palaeoclimatology, Palaeoecology, v. 291, p. 11–39, https://doi.org/10.1016/j.palaeo.2009.12.012.
Shen, J., Chen, J.B., Algeo, T.J., Yuan, S.L., Feng, Q.L., Yu, J.X., Zhou, L., O'Connell, B., and Planavsky, N.J., 2019a, Evidence for a prolonged Permian–Triassic extinction interval from global marine mercury records: Nature Communications, v. 10, 1563, https://doi.org/10.1038/s41467-019-09620-0.
Shen, J., et al., 2019b, Mercury evidence of intense volcanic effects on land during the Permian-Triassic transition: Geology, v. 47, p. 1117–1121, https://doi.org/10.1130/G46679.1.Shen, S.Z., et al., 2011, Calibrating the end-Permian mass extinction: Science, v. 334, p. 1367–1372, https://doi.org/10.1126/science.1213454.
Shen, S.Z., et al., 2011, Calibrating the end-Permian mass extinction: Science, v. 334, p. 1367–1372, https://doi.org/10.1126/science.1213454.
Shen, S.Z., et al., 2019, A sudden end-Permian mass extinction in South China: Geological Society of America Bulletin, v. 131, p. 205–223, https://doi.org/10.1130/B31909.1.
Song, H.J., Wignall, P.B., Tong, J.N., and Yin, H.F., 2013, Two pulses of extinction during the Permian-Triassic crisis: Nature Geoscience, v. 6, p. 52–56, https://doi.org/10.1038/ngeo1649.
Them, T.R., II, Jageo, C.H., Caruthers, A.H., Gill, B.C., Grabsy, S.E., Gröcke, D.R., Yin, R., and Owens, J.D., 2019, Terrestrial sources as the primary delivery mechanism of mercury to the oceans across the Toarcian Oceanic Anoxic Event (Early Jurassic): Earth and Planetary Science Letters, v. 507, p. 62–72, https://doi.org/10.1016/j.epsl.2018.11.029.
Wang, X.D., Cawood, P.A., Zhao, H., Zhao, L.S., Grasby, S.E., Chen, Z.Q., Wignall, P.B., Li, Z., and Han, C., 2018, Mercury anomalies across the end Permian mass extinction in South China from shallow and deep water depositional environments: Earth and Planetary Science Letters, v. 496, p. 159–167, https://doi.org/10.1016/j.epsl.2018.05.044.
Wang, X., Cawood, P.A., Zhao, H., Zhao, L., Grasby, S.E., Chen, Z.Q., and Zhang, L., 2019, Global mercury cycle during the end-Permian mass extinction and subsequent Early Triassic recovery: Earth and Planetary Science Letters, v. 513, p. 144–155, https://doi.org/10.1016/j.epsl.2019.02.026.
Wignall, P.B., 2001, Large igneous provinces and mass extinctions: Earth-Science Reviews, v. 53, p. 1–33, https://doi.org/10.1016/S0012-8252(00)00037-4.
Wignall, P.B., 2015, The Worst of Times: How Life on Earth Survived Eighty Million Years of Extinction: Princeton, New Jersey, Princeton University Press, 224 p.
Zhang, H., Cao, C.Q., Liu, X.L., Mu, L., Zheng, Q.F., Liu, F., Xiang, L., Liu, L.J., and Shen, S.Z., 2016, The terrestrial end-Permian mass extinction in South China: Palaeogeography, Palaeoclimatology, Palaeoecology, v. 448, p. 108–124, https://doi.org/10.1016/j.palaeo.2015.07.002.

Printed in USA